University of Dundee

Construction of perovskite solar cells using inorganic hole-extracting components

Nouri, Esmaiel; Mohammadi, Mohammad Reza; Lianos, Panagiotis

Link to publication in Discovery Research Portal

Download date: 01. May. 2020

Construction of Perovskite Solar Cells Using Inorganic Hole-Extracting Components

Esmaiel Nouri,[†] Mohammad Reza Mohammadi,[*,†] and Panagiotis Lianos[*,‡]

[†]Department of Materials Science and Engineering, Sharif University of Technology, Azadi Street, 11369 Tehran, Iran

[‡]Department of Chemical Engineering, University of Patras, 26500 Patras, Greece

ABSTRACT: A NiO_x−graphene oxide (NiO_x−GO) hybrid has been prepared by a simple solution-processed method and was used as hole-extraction material in perovskite solar cells with either gold or carbon as back contact electrode. The impact of GO content on the optoelectronic behavior of NiO_x and the photovoltaic performance of the fabricated devices has been studied. Thus, GO incorporation showed a significant improvement in the performance of NiO_x-based devices. The best attained efficiency was 13.3%, and it was 45% higher than that with pure NiO_x. This is attributed to a significant improvement in the hole extraction, recombination resistance, and energy-level matching in comparison to pure NiO_x. In addition, NiO_x−GO/Au-based perovskite solar cell devices showed a negligible hysteresis effect and high reliability and repeatability. When carbon was used as back contact electrode, the obtained efficiencies were lower, but it leaves space for improvement. Devices based on inorganic hole transporters NiO_x or NiO_x−GO demonstrated higher stability in ambient air compared to a standard cell based on spiro-OMeTAD.
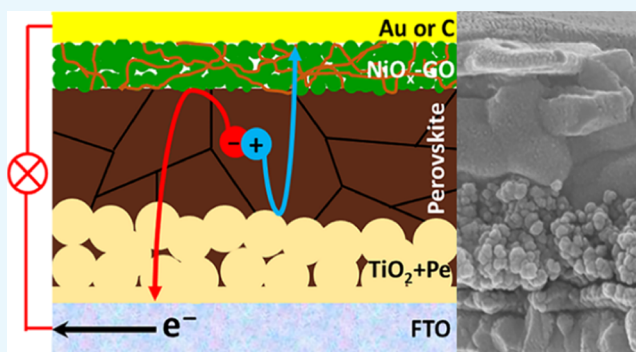
INTRODUCTION

Organometal halide perovskite solar cells (PSCs), which is the youngest technology in solar energy conversion, have incited very high interest among a large number of researches by exhibiting very high power-conversion efficiency (PCE) >22%.[1] Such an amazing performance is due to the excellent optoelectronic characteristics of the hybrid organic−inorganic perovskite, which acts as light harvester. Among these properties is its high light absorption coefficient at room temperature, charge accumulation in high density of states,[2] very high electron−hole diffusion lengths,[3,4] no optically detectable deep states,[5] and high charge-carrier mobility.[6,7] Mesoscopic PSC devices are grown on a transparent electrode (usually, fluorine-doped tin oxide, FTO) by first depositing a mesoporous scaffold (typically, TiO_2 or Al_2O_3), followed by a perovskite light absorber, a high-purity organic hole-transporting material (HTM), typically spiro-OMeTAD, and a noble metal electrode (Au or Ag). The PSC devices with the above configuration are very expensive because of the high cost of spiro-OMeTAD and of the noble metal back contact. In addition to their high cost, applying metal electrodes on PSC devices requires a high-vacuum and costly evaporation installation, limiting their future commercial application. It is clear that to overcome these cost-limiting problems, the expensive components should be replaced or removed. In this respect, we have proposed soluble n-butyl-substituted copper phthalocyanine[8] and soluble tetratriphenylamine Zn phthalocyanine[9] as promising soluble candidates for spiro-OMeTAD substitution. However, it is broadly illustrated and

discussed in the literature that there are other limiting factors (besides high cost) brought about by metal back contact and organic hole conductors in PSCs. Thus, metal migration[10] as well as moisture- and illumination-induced degradation of organic components[11] is of primary concern with PSCs. Migration of metal inside the perovskite film can create shunt paths across the cell and also deep trap states within the semiconductor, leading to reduction of fill factor (FF). In addition, enhancement of nonradiative recombination is accompanied by lower open-circuit voltage (V_{OC}) and short-circuit current density (J_{SC}).[10,12] One solution to control metal-migration-induced degradation is application of a buffer layer between hole conductor and perovskite films.[12−14] We have applied graphene oxide (GO) buffer layer infiltrated with HTM to suppress metal-atom penetration into the perovskite layer during aging.[8] On the other hand, moisture and illumination can drastically degrade the organic components.[15] Such degradation can affect the long-term stability of PSCs under ambient air conditions, and this constitutes the biggest challenge faced by organic components for realistic applications of PSC devices.[16]

In recent years, inorganic carbonaceous materials have been attracting substantial attention as promising alternatives to the organic components, thanks to their stability, abundancy, and cost reduction of fabrication procedure via paintable or
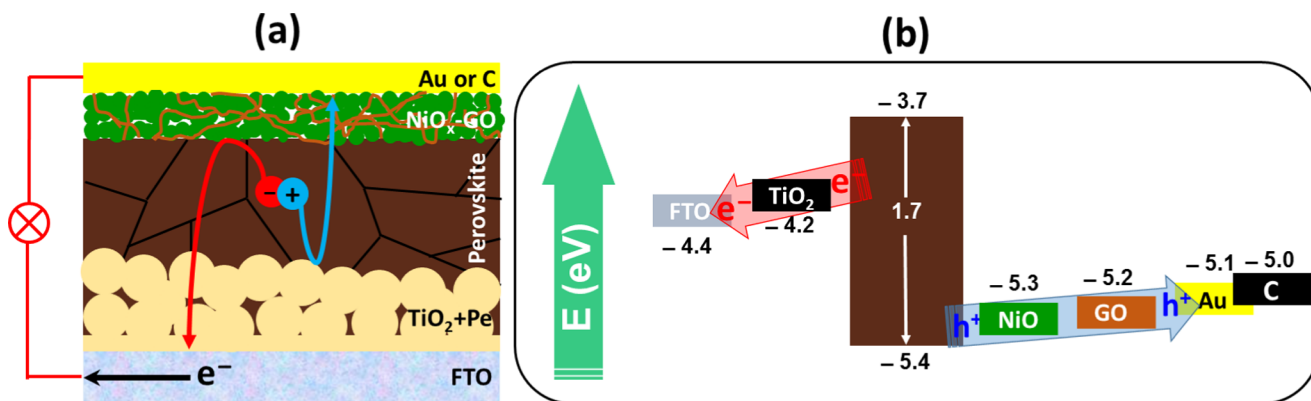
Figure 1. (a) Schematic illustration of the NiO$_x$−GO-based PSC device and (b) energy-level diagram showing charge flow in the device. Energy levels have been borrowed from our previous works.[20,21]

printable depositions.[7−19] Thanks to the hydrophobic nature of carbonaceous materials, they may also discourage humidity penetration. Our concept was to replace the unstable organic components by constructing inverted PSCs with graphene derivatives (i.e., graphene oxide and lithium-functionalized graphene oxide as hole- and electron-transporting layers, respectively).[20,21] However, there are still other choices to make. Thus, in the present work, we have succeeded in constructing functional cells by completely eliminating organic hole transporters and by substituting them with a NiO$_x$−GO blend. The choice of NiO$_x$ was dictated by its favorable properties. It is a p-type semiconductor and thus may be used as hole transporter. Its energy level is favorably located to be combined with organometal halide perovskites (cf. Figure 1) and is easily synthesized by solution processes at low temperature; therefore, it may be nondestructively deposited on the perovskite film.[22,23] However, its photovoltaic performance is limited by its low intrinsic conductivity ($10^{−4}$ S/cm).[24] For this reason, NiO$_x$ has been, for example, doped with metals to increase its conductivity.[24,25] In the present work, we have opted for NiO$_x$−GO combinations, which proved out to be a successful choice. The device structure was completed by a metal or a carbon back electrode. Device construction and characterization was carried out under ambient conditions of 28−32% relative humidity. The achieved efficiencies were lower than those obtained with organic hole transporters. However, all factors taken into account, the present approach might come out to be much more realistic and thus more promising. The easiness of cell construction, which will emerge from the present data, will by itself bring support to this assertion.

RESULTS AND DISCUSSION

The data listed in this work refer to PSC devices which were made using inorganic components with a principal role played by carbonaceous materials. Devices were constructed and tested first using a Au and then a carbon back contact electrode. As explained in the Experimental Procedures section, the NiO$_x$−GO mixtures used in the present work are abbreviated as NiO$_x$−1GO, NiO$_x$−2GO, NiO$_x$−3GO, and NiO$_x$−4GO. The numbers in front of GO correspond to the added multiple of a unit quantity of GO.

Figure 1 illustrates the energy band alignment together with a schematic configuration of the NiO$_x$−GO-based PSC devices, which have been studied in this work. The work function and the corresponding energy levels of device components have been obtained in our previous works.[20,21] As shown in Figure 1a, electron−hole pairs are generated when incident photons are absorbed by the photoactive perovskite film. Then, electrons are transferred to the transparent FTO substrate, whereas holes are extracted by the back Au or carbon terminals. Electron- and hole-extraction layers (EEL and HEL, respectively) are necessary at the interface between the perovskite film and the electrodes to reduce the developing energy barriers and suppress interfacial charge recombination. In addition, the output V_{OC} is a function of the energy-level difference of electron transport layer (ETL) and hole transport layer (HTL). It is obvious from Figure 1b that there is a perfect matching of the energy levels, which guarantees cell functioning.

The actual deposited materials and the formation of layers during device construction were characterized by transmission electron microscopy (TEM) and field emission scanning electron microscopy (FESEM). The FESEM and TEM images in Figure 2a,b, respectively, show the as-synthesized NiO$_x$−GO hybrids. It can be seen from the FESEM image in Figure 2a that a heavy NiO$_x$ nanoparticles loading on GO sheets was obtained. As revealed by the inset of Figure 2b, the sizes of the NiO$_x$ nanoparticles are in the range of 5−10 nm. Energy-dispersive X-ray spectrometry (EDS) mapping of the NiO$_x$−GO hybrids was conducted to analyze their chemical composition and further confirm the uniformity of the distribution of GO carbonaceous sheets in NiO$_x$ nano-particulate matrix. Figure 2c−e shows the distribution of Ni, O, and C elements in the NiO$_x$−GO blend, respectively, indicating a satisfactory dispersion of components within the hybrid. Crystallinity of the obtained pure NiO$_x$ and NiO$_x$−3GO nanoparticulate hybrids was characterized by X-ray diffraction (XRD) analysis. As shown in Figure 2f, both samples exhibit three main Bragg diffraction peaks at 2θ of 37.3, 43.6, and 62.8°, which can be, respectively, assigned to the (111), (200), and (220) planes, suggesting a cubic crystalline structure (PDF: 47-1049). Obviously, only NiO$_x$ contributes to the detected diffraction peaks.

The morphology of the perovskite film fabricated on mesoporous TiO$_2$ layer is shown in Figure 3a. We can observe a continuous, flat, and full-coverage film with large grains, which guarantee the perovskite crystallite formation and subsequently the PSC device functioning. Figure 3b depicts a fully covered compact structure of the NiO$_x$−3GO film without voids (i.e., no perovskite can be seen through this film). This helps to control metal-migration-induced degradation, which may damage the layer underneath by creating shunt paths between
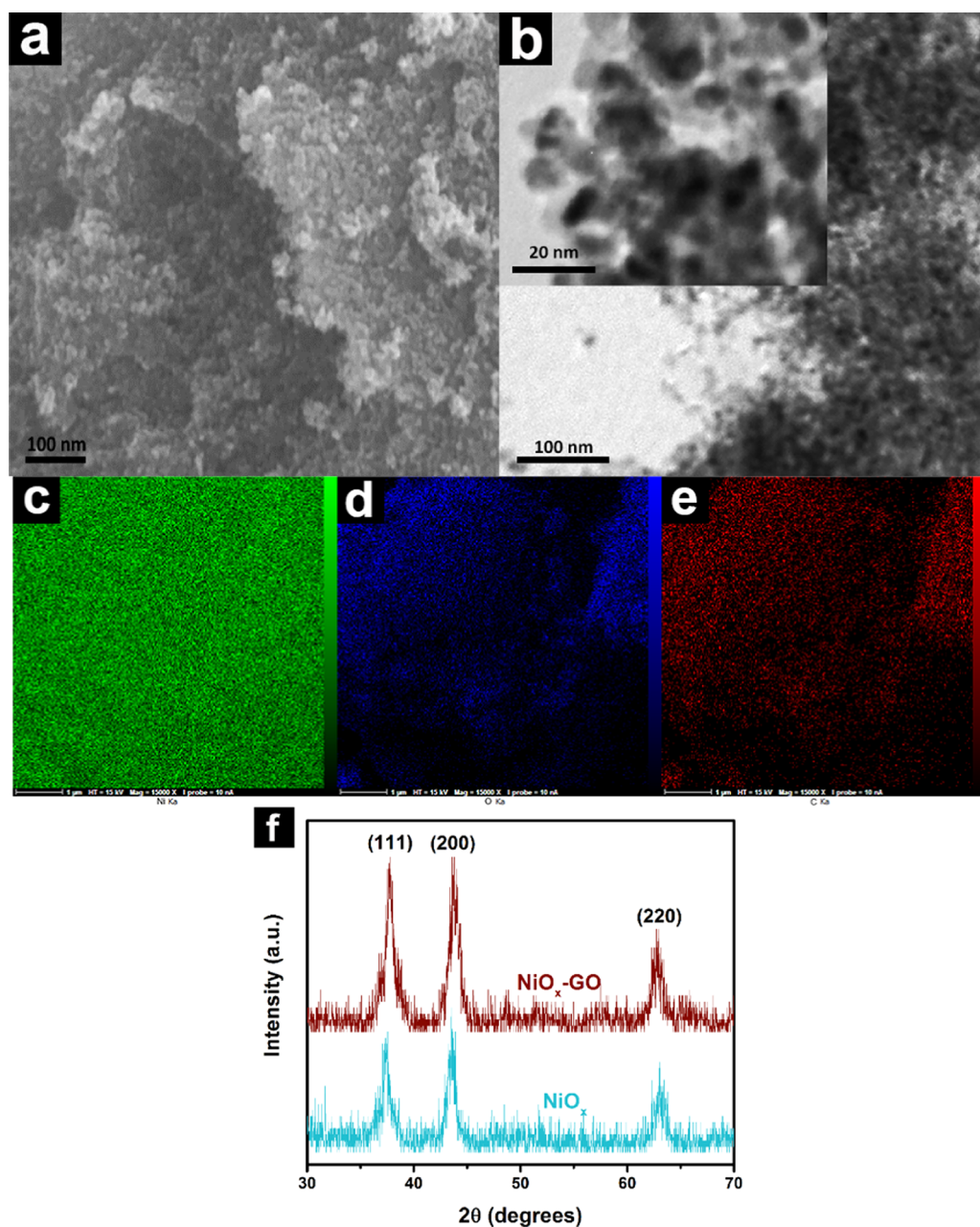
Figure 2. (a) SEM, (b) TEM images, and EDS mapping of (c) Ni, (d) O, and (e) C elements in the NiO$_x$−3GO hybrid. The scale bar is 1 μm in all EDS maps. (f) XRD patterns of pure NiO$_x$ and NiO$_x$−3GO hybrid films.

the perovskite layer and the back contact electrodes. A typical cross-sectional FESEM image of the PSC device is demonstrated in Figure 3c, showing a configuration of FTO/TiO$_2$ compact layer/TiO$_2$ mesoporous layer/perovskite film/NiO$_x$−3GO/Au. The most interesting characteristic of this image is the fact that a continuous and compact hole-extraction layer of NiO$_x$−3GO has been obtained, and this was achieved with a simple solution-processed procedure.

Figure 4 shows J−V and incident photon-to-charge carrier efficiency (IPCE) curves of PSC devices with Au back contact electrode under both forward and reverse scans with pure NiO$_x$ and NiO$_x$-incorporated graphene oxide as hole-extracting layer (HEL). For the NiO$_x$−3GO/Au-based device, a PCE of 13.3% was obtained under forward scan, where J_{SC}, V_{OC}, and FF were 20.4 mA/cm^2, 1.03 V, and 0.63, respectively. However, the control device with pure NiO$_x$/Au layer exhibited a J_{SC} of 19.0

mA/cm^2, a V_{OC} of 0.95 V, and a FF of 0.51, resulting in a PCE of 9.2% under forward scan. It is noteworthy that the NiO$_x$/Au-based device demonstrated a serious hysteresis effect, which may be attributed to the inefficient hole extraction from the perovskite film to the NiO$_x$ layer. However, in the presence of GO, such obstacles were overcome so that the NiO$_x$−GO/Au-based PSC devices had a negligible hysteresis effect, indicating that the GO sheets markedly improved the charge-collection capacity.

Corresponding photovoltaic characteristics of the cells made by using carbon as back contact electrode are presented in Figure 5 and Tables 1 and 2. All photovoltaic parameters reached lower values than in the case of gold. Especially, the fill factor and the open-circuit voltage suffered large losses. This lower performance is due to different conductive characteristics of carbon compared to gold, as well as to the porous structure
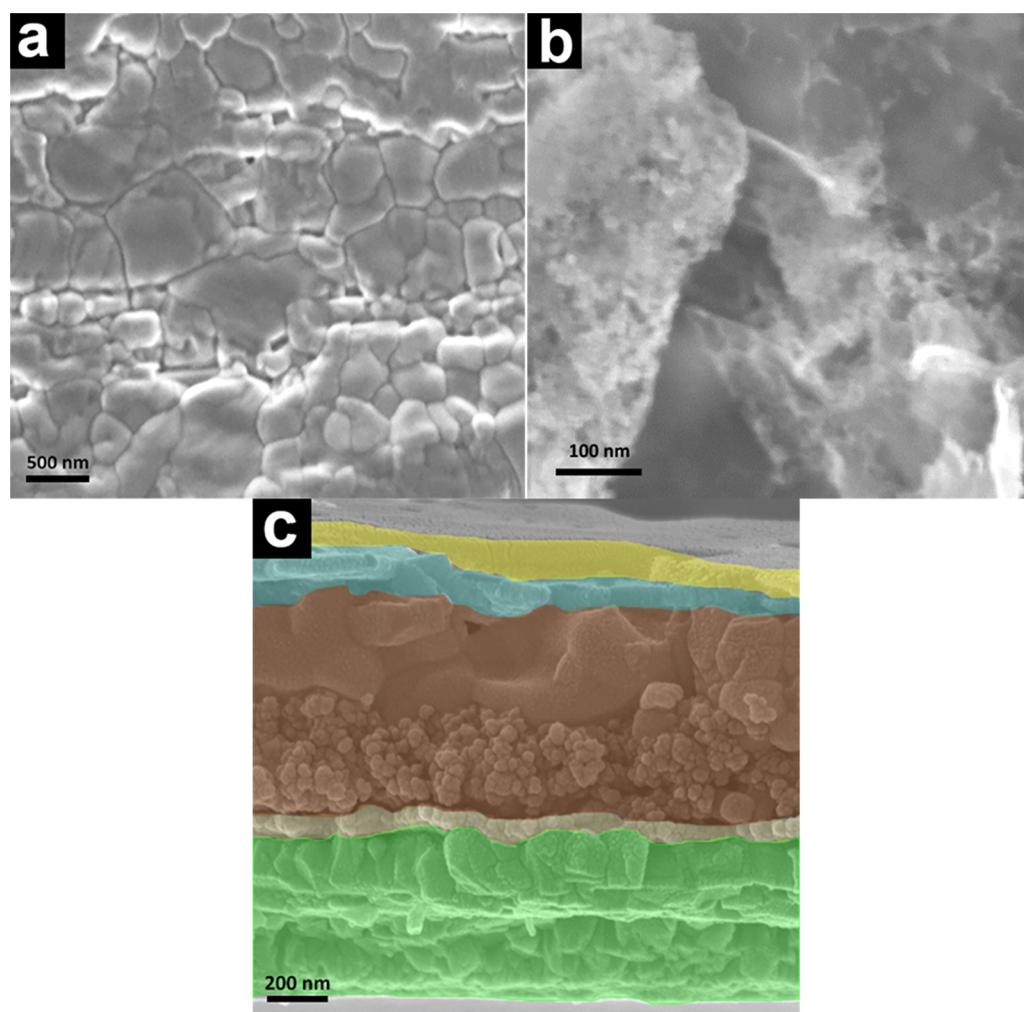
Figure 3. FESEM top views of (a) perovskite film applied on a TiO_2 mesoporous layer and (b) NiO_x−3GO nanoparticulate film on top of the perovskite film. (c) Cross-sectional FESEM image of the subsequent layers making the PSC device based on NiO_x−3GO hole-extraction layer with a configuration of FTO/TiO_2 compact layer/TiO_2 mesoporous layer/perovskite film/NiO_x−3GO/Au.

Figure 4. Photovoltaic metrics of PSCs made by NiO_x/Au and NiO_x−GO/Au hole-extraction layers: (a) Current density−voltage (J−V) curves under forward and reverse scans and (b) incident photon-to-carrier efficiency spectra (left ordinate) and photocurrent density (right ordinate) calculated by integrating the corresponding IPCE spectra under AM 1.5 simulated sunlight.
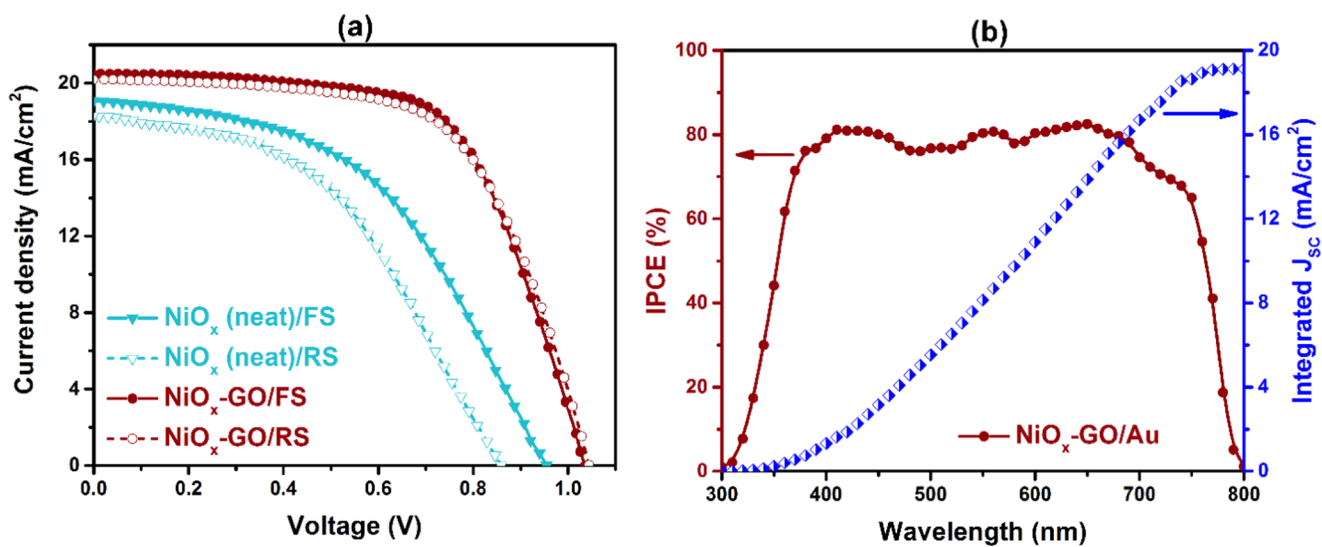
Figure 5. Photovoltaic metrics of PSCs made by NiO$_x$/carbon and NiO$_x$–GO/carbon hole-extraction layers: (a) current density–voltage ($J–V$) curves under forward and reverse scans and (b) incident photon-to-carrier efficiency spectra (left ordinate) and photocurrent density (right ordinate) calculated by integrating the corresponding IPCE spectra under AM 1.5 simulated sunlight.
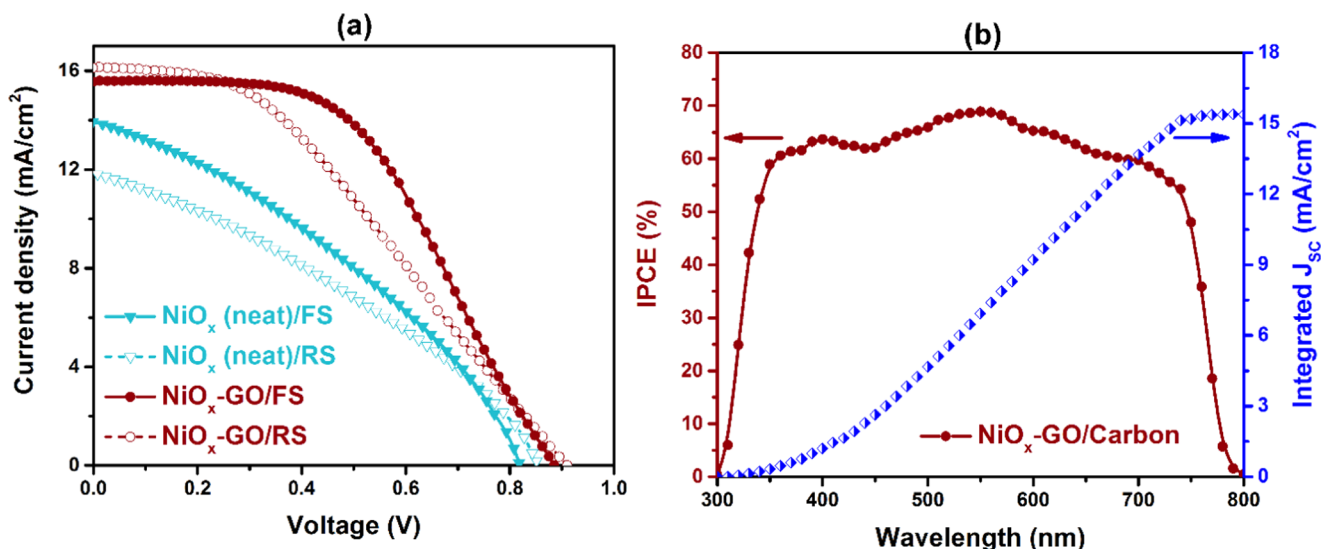
Table 1. Photovoltaic Parameters of the NiO$_x$- and NiO$_x$–GO-Based PSC Devices with Au as Back Contact Electrode Measured under Simulated AM 1.5 (100 mW/cm^2) Conditions

hole-extraction layer	J_{SC} (mA/cm^2)	V_{OC} (V)	FF	η (%)
NiO$_x$ (neat)	19.0 ± 0.51	0.95 ± 0.023	0.51 ± 0.032	9.2 ± 0.75
NiO$_x$–1GO	19.5 ± 0.36	0.98 ± 0.006	0.60 ± 0.020	11.5 ± 0.56
NiO$_x$–2GO	20.2 ± 0.22	0.99 ± 0.021	0.62 ± 0.027	12.4 ± 0.76
NiO$_x$–3GO	20.4 ± 0.30	1.03 ± 0.019	0.63 ± 0.022	13.3 ± 0.66
NiO$_x$–4GO	20.4 ± 0.19	1.01 ± 0.026	0.61 ± 0.030	12.6 ± 0.87

Table 2. Photovoltaic Parameters of the NiO$_x$- and NiO$_x$–GO-Based PSC Devices with Carbon as Back Contact Electrode Measured under Simulated AM 1.5 (100 mW/cm^2) Conditions

hole-extraction layer	J_{SC} (mA/cm^2)	V_{OC} (V)	FF	η (%)
NiO$_x$ (neat)	13.9 ± 0.26	0.82 ± 0.052	0.34 ± 0.037	4.1 ± 0.59
NiO$_x$–1GO	14.6 ± 0.62	0.86 ± 0.021	0.42 ± 0.032	5.3 ± 0.75
NiO$_x$–2GO	14.8 ± 0.30	0.86 ± 0.010	0.48 ± 0.023	6.1 ± 0.38
NiO$_x$–3GO	15.6 ± 0.51	0.88 ± 0.023	0.51 ± 0.032	7.0 ± 0.75
NiO$_x$–4GO	15.8 ± 0.98	0.87 ± 0.014	0.52 ± 0.013	7.1 ± 0.59

of the carbon layer. However, we believe that this is a matter of optimization and therefore there is room for improvement.

To better understand hole-extraction functionality by the NiO$_x$–GO layer, UV–vis and photoluminescence (PL) spectra of the perovskite films on NiO$_x$ and NiO$_x$–GO layers deposited on FTO substrates were studied and are presented in Figure 6. The UV–vis absorption spectra (Figure 6a) show a much higher absorbance in the range of 400–750 nm for NiO$_x$ and NiO$_x$–GO-containing films, compared to neat perovskite as reference sample. The corresponding steady-state photoluminescence spectra, illustrated in Figure 4b, show a perovskite film luminescence peak at 709 nm. In the presence of NiO$_x$, photoluminescence was substantially quenched, indicating charge transfer between NiO$_x$ and perovskite photoactive layer. It is interesting to note that photoluminescence quenching was even more extensive in the presence of GO. These data then indicate that charge transfer between the photoactive layer and the hole-extracting layer is effective and it is even more so in the presence of GO.

An obvious question may then be asked as to the nature of the support brought about by the presence of GO. Both NiO$_x$ and GO are not thermally treated; therefore, NiO$_x$ exact stoichiometry cannot be assured and GO is not transformed into reduced graphene oxide. Thus, the presence of GO cannot offer higher conductivities to the layer. This matter has been studied by electrochemical impedance spectroscopy (EIS) measurements. Figure 7 shows EIS data and the insets present the equivalent circuit models. By fitting Nyquist plots, the total series resistance (R_s) of the devices was calculated to be around 11 Ω. The closeness in R_s values in all devices was due to the similar device structure, as shown in Figure 1. However, an obvious difference was observed with the charge-transfer resistance (R_t) values at the ETL/perovskite or HTL/perovskite interface between devices made with neat NiO$_x$ and devices made with the optimal NiO$_x$–GO layer (i.e., NiO$_x$–3GO). Figure 7a shows the corresponding Nyquist plots under dark and at a bias of V_{OC}, exhibiting internal charge transport and recombination through the PSC devices. Only one semicircle could be distinguished in the Nyquist plots,
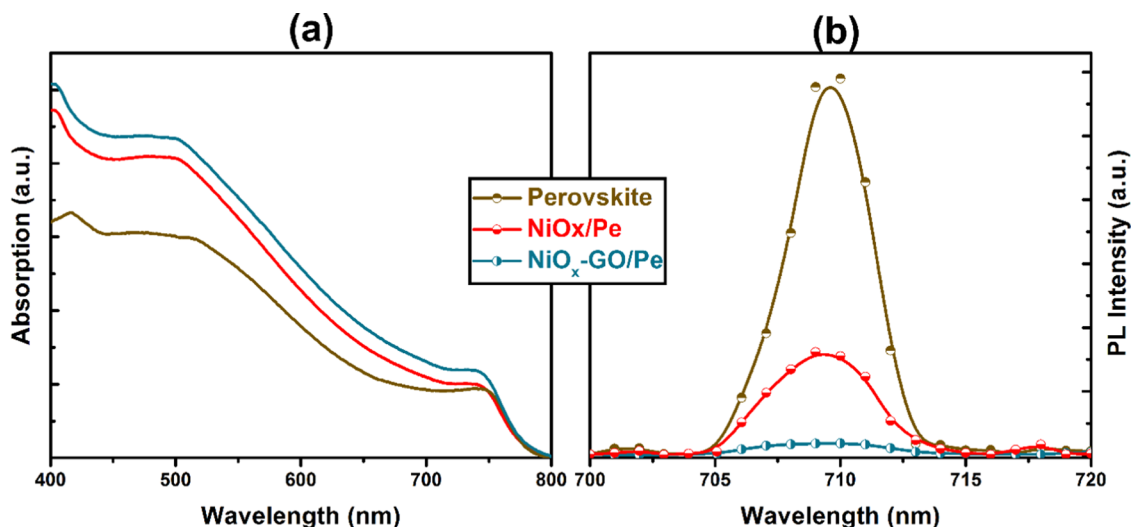
Figure 6. (a) UV−vis absorption and (b) photoluminescence spectra of the perovskite films on NiO$_x$ and NiO$_x$−GO layers deposited on FTO substrates. Photoluminescence was recorded by excitation at 450 nm.
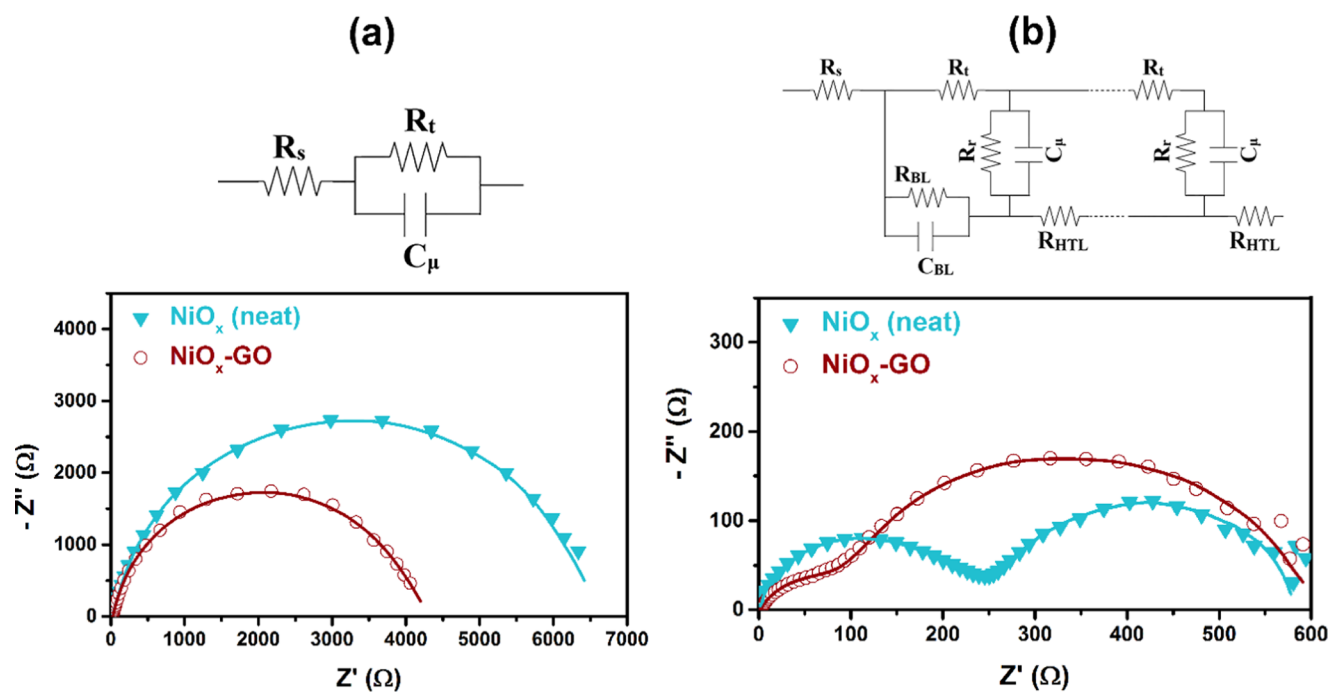

Figure 7. Nyquist plots and equivalent circuits for fitting the EIS data of the NiO$_x$- and the NiO$_x$−GO-based PSC devices measured under (a) dark and (b) AM 1.5G illumination conditions with a bias voltage of V_{OC}. The solid lines are the fitted curves. On the transmission line equivalent circuit used to fit the impedance data, R_s represents the resistance of conductive substrate, C_{BL} is the capacitance, R_{BL} is the charge-transfer resistance at TiO$_2$ compact blocking layer, R_t is the transport resistance at the ETL/perovskite or the HTL/perovskite interface, R_r is the recombination resistance accounting for losses of electrons from perovskite absorber layer, C_μ is the chemical capacitance, and R_{HTL} is the resistance of NiO$_x$ or NiO$_x$−GO as hole-transporting materials.

attributed to charge-transfer resistance (R_t) at the interface between NiO$_x$ or NiO$_x$−GO and perovskite film. The NiO$_x$−GO-based PSC devices had lower R_t, i.e., smaller semicircle, than the control device with neat NiO$_x$ as HTL. The smaller R_t implies a faster charge transport at the interface of HEL/perovskite. This result confirms the conclusions drawn by the above photoluminescence measurements, as shown in Figure 6b. Nyquist plots of the cells measured under AM 1.5G illumination conditions and the equivalent circuit are shown in Figure 7b, where both high- and low-frequency semicircles become evident. The high-frequency part of the spectra

contains information on charge-transfer resistance (R_t) and series resistance (R_s) elements, as well as dielectric contributions.[26] The low frequency arc is attributed to recombination resistance (R_r) at the photoactive layer.[27] By fitting the Nyquist plot with an equivalent circuit, the NiO$_x$−GO-based device shows a smaller value of R_t and a larger value of R_r (i.e., interfacial recombination resistance). The more efficient hole-extraction process from perovskite photoactive layer and the more efficient suppressing of charge recombination in the case of NiO$_x$−GO-based PSC device resulted in a better device performance, compared to the neat NiO$_x$-based device. To

answer then the question at the beginning of this paragraph, we may conclude that the presence of GO does not support higher conductivity, thus leaving series resistance unaffected, but offering a better structural organization of the HEL facilitates charge transfer while impeding charge recombination.

The photoconversion efficiency vs time curves for the corresponding PSC devices based on spiro-OMeTAD (as reference standard HTL) and for the above NiO_x and NiO_x–3GO devices with either Au or carbon back contact electrodes are compared in Figure 8. The devices were kept in a dry box of
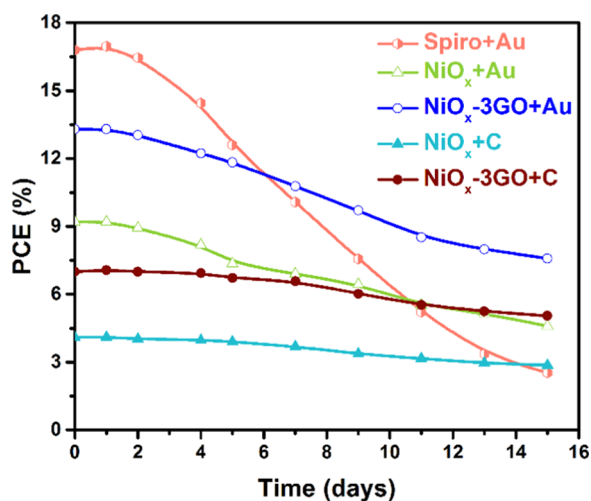

Figure 8. Photoconversion efficiency as a function of aging time of PSC devices based on spiro-OMeTAD, NiO_x, and NiO_x–3GO as hole-extraction layers with Au and carbon back contacts.

relative humidity 28−32% under dark conditions and then their photovoltaic performance was measured at different time intervals under ambient air at room temperature. Comparison of performance of different HTL components indicated that the photoconversion efficiency of the spiro-based PSCs underwent intensive more rapid deterioration in a period of a few days and reached nearly a dead point, with only 14% of its initial PCE remaining, after 15 days of device operation. During the same period of time, the NiO_x–3GO component significantly delayed the photoinduced degradation, thereby retaining about 72% (carbon electrode) and 57% (Au electrode) of the initial photoconversion efficiency after 15 days of device operation. It is noteworthy that in the beginning of the aging test spiro-based device exhibited 27% higher PCE than the best-performance device based on NiO_x–3GO. But after about 6 days of their initial operations, they had the same PCE of 11.2% and then the inorganic-based PSC showed a better performance. This indicates that the oxygen and moisture apparently deteriorate all fabricated PSC devices, but those with NiO_x HTL show distinctly more stable behavior, especially in the presence of graphene oxide. This may be attributed to the good shielding role of NiO_x−GO hybrids against the penetration of humidity into the highly sensitive perovskite layer under ambient conditions.

One more interesting point in Figure 8 is the impact of back contact electrode material on long-term stability of PSCs. If we consider a certain HTL (NiO_x or NiO_x–3GO) with different carbon and Au back contact electrodes, it is not surprising that Au caused more rapid deterioration of PCE than carbon back contact. Metal can migrate inside the perovskite film during device operation and create shunt paths across the cell.[10] This

seems to be less probable in the case of carbon. In addition, carbon layer adds to the protective effect brought about by its hydrophobic nature.

CONCLUSIONS

Perovskite solar cells have been constructed using solution-processable inorganic components with NiO_x−GO blends making the hole-extraction layer. Devices have been made and characterized under ambient conditions of 28−32% relative humidity. The obtained maximum efficiency was lower than the values reported with organic hole-transporting materials; however, with all factors taken into account, the proposed route might come out to be much more realistic and thus more promising. Moreover, these devices showed a higher stability in ambient air compared to a standard PSC device based on spiro-OMeTAD. Devices have been constructed by easy procedures, and this is particularly true for the deposition of the NiO_x−GO layer, which was functional despite the simplicity of synthesis and deposition. GO does not increase conductivity as has been observed with metal-doped NiO_x, but its presence apparently helps to organize the hole-extraction layer and thus increase its functionality.

EXPERIMENTAL PROCEDURES

Materials. All reagents were purchased from Sigma-Aldrich, unless otherwise specified, and used as received. SnO_2:F transparent conductive substrates (FTO, resistance 7 Ω/square) (TCO22-7) and carbon paste were purchased from Solaronix. Commercial Degussa P25 was used for the preparation of homemade TiO_2 paste used for the deposition of the mesoporous titania layer.

Preparation of GO, NiO_x, and NiO_x−GO. Full details of GO synthesis have been reported in our previous work.[28] Briefly, GO was synthesized on the basis of the Hummers and Offeman method,[29] involving two steps: preoxidation of graphite flakes and exfoliation of graphene oxide. In the first step, $K_2S_2O_8$ and P_2O_5 were utilized as oxidizing agent of graphite flakes in concentrated H_2SO_4 at 80 °C. In the second step, the above oxidized graphite powder underwent progressive oxidation and exfoliation using $KMnO_4$ and $NaNO_3$ in a cooled H_2SO_4 bath. Deionized water was added into the mixture to increase the oxidation degree of the GO product. Residual oxidizing agents were dissolved with 30% H_2O_2. The gross product was treated with 10% HCl solution in ethanol and deionized water to eliminate the residual metal ions. The yellow-brown GO dispersion was then subjected to dialysis to completely remove metal ions and acids. Finally, it was dehydrated in an air oven to yield the GO powder. In the next step, a dispersion of the GO sheets in isopropanol and glacial acetic acid with a concentration of 5 mg/mL were prepared using an ultrasonic bath. The resultant homogeneously exfoliated suspensions were used as graphene source to synthesize NiO_x−graphene oxide (NiO_x−GO) hybrids via a simple solution-processed method as follows. Nickel(II) nitrate hexahydrate ($Ni(NO_3)_2 \cdot 6H_2O$, 1.5 g) was added to 50 mL of isopropanol and stirred overnight. The resultant green NiO_x precursor solution was filtered using a porous poly-(tetrafluoroethylene) membrane filter (0.45 μm). To prepare NiO_x−GO hybrids with different contents of GO, four different amounts (1, 2, 3, and 4 mL) of the above prepared GO dispersion were added dropwise into 10 mL of NiO_x precursor solution in isopropanol under stirring, followed by 10 min

sonication. The obtained NiO_x–GO mixtures are abbreviated as NiO_x–1GO, NiO_x–2GO, NiO_x–3GO, and NiO_x–4GO, respectively. The numbers in front of GO correspond to the added amounts (mL) of GO dispersion, and because the content of the latter in GO was 5 mg/mL, it is expected that the quantity of GO in the mixture was equal to the corresponding multiples of 5 mg (i.e., 5, 10, 15, and 20 mg, respectively).

Construction of PSC Devices. FTO-coated glass substrates were cut in pieces of dimensions 1 cm × 3 cm. One-third of the conductive layer was etched using zinc powder and hydrochloric acid. They were washed with mild detergent, rinsed several times with distilled water and subsequently with ethanol and acetone in an ultrasonic bath, and finally dried under air stream. A compact thin layer of TiO_2 was then deposited on this patterned and cleaned FTO electrode by aerosol spray pyrolysis using a solution of 0.2 M diisopropoxytitanium bis(acetylacetonate) in ethanol. After spraying, the samples were dried for 10 min at 100 °C and heated for 1 h at 500 °C. Subsequently, a mesoporous TiO_2 layer was spin-coated at 4000 rpm for 60 s using a TiO_2 paste made of P25 nanoparticles. The obtained film was dried at 100 °C for 20 min and calcined for 30 min at 500 °C. After that, the samples were treated in $TiCl_4$ by dipping into a solution made of 0.04 M $TiCl_4$ in H_2O for 30 min at 70 °C, then copiously rinsing, and finally calcining at 500 °C. Active perovskite layer was deposited on mesoporous TiO_2 film by the following procedure. PbI_2 (507 mg) and $PbCl_2$ (253 mg) were dissolved in 1.5 mL of dimethylsulfoxide (DMSO) at 170 °C. After cooling at room temperature, 270 mg of methyl ammonium iodide was added under stirring. The solution was kept under stirring for about 2 h at about 80 °C and then deposited by two consecutive spin-coating steps: first 1000 rpm for 10 s and then 6000 rpm for 30 s. During the second step, 1 mL of chlorobenzene, as an antisolvent, was gently dropped on the spinning substrate. The layer was then heated at 90 °C for about 45 min, which made the sample's color turn from yellow to black. Thereafter, NiO_x or NiO_x–GO as hole-extraction layer was spin-coated from its stock solution at 3000 rpm for 40 s directly on the annealed perovskite layer at room temperature, followed by heating at 100 °C for 10 min. All procedures were carried out under ambient conditions of 28−32% relative humidity. The last step for preparing the PSC devices was the deposition of back contact electrode. Two different procedures and materials were used for this purpose. First, 90 nm thick gold electrodes were deposited by thermal evaporation under vacuum. In the second case, carbon electrodes were constructed by screen-printing a commercial carbon paste on NiO_x or NiO_x–GO layers and dried at 100 °C for 10 min. Two unit devices were made in each case with an active size of 15 mm^2 (10 mm × 1.5 mm) as defined by the size of gold or carbon electrodes.

Characterization and Measurements. The size and morphology of NiO_x nanoparticles blended with GO sheets were analyzed by transmission electron microscopy (TEM/JEOL, JEM-2100, Japan) operating at 200 kV. Solar cell devices configuration and subsequent layers' morphology were imaged by means of field emission scanning electron microscopy (FESEM, MIRA3 TESCAN, Czech Republic) with a field emission gun equipped with an energy-dispersive X-ray spectrometry (EDS) system. The UV−vis absorbance properties of mesoporous layers were recorded using an AVASPEC-2048-TEC instrument (Avantes, The Netherlands). Photo-

luminescence (PL) spectra were recorded on a Cary Eclipse fluorescence spectrometer. The photovoltaic parameters of the PSC devices were studied using a Zahner Cimps PCS solar simulator (Zahner, Kronach, Germany) set at 100 mW/cm^2. The devices were illuminated through a mask of aperture size 1 mm × 6 mm under ambient conditions at a scan rate of 50 mV/s. Incident photon-to-charge carrier efficiency (IPCE) was obtained using a setup with a Jarrell-Ash monochromator, a 100 W halogen lamp, and a calibrated photodiode (Thorlabs). Electronic impedance spectroscopy (EIS) characterization was carried out with a potentiostat/galvanostat (PGSTAT128N, Autolab B.V., The Netherlands) under both dark and AM 1.5G illuminated conditions at a frequency range of 1 Hz to 3 MHz.

■ AUTHOR INFORMATION

Corresponding Authors
*E-mail: mohammadi@sharif.edu (M.R.M.).
*E-mail: lianos@upatras.gr (P.L.).

ORCID ⊙
Mohammad Reza Mohammadi: 0000-0001-7999-3233
Panagiotis Lianos: 0000-0003-3955-0272

Notes
The authors declare no competing financial interest.

■ REFERENCES

(1) NREL Chart Homepage. https://www.nrel.gov/pv/assets/images/efficiency-chart.png (accessed Oct, 2017).
(2) Kim, H. S.; Sero, I. M.; Pedro, V. G.; Santiago, F. F.; Perez, E. J. J.; Park, N. G.; Bisquert, J. Mechanism of Carrier Accumulation in Perovskite Thin-Absorber Solar Cells. *Nat. Commun.* **2013**, *4*, No. 2242.
(3) Dong, Q.; Fang, Y.; Shao, Y.; Mulligan, P.; Qiu, J.; Cao, L.; et al. Electron-Hole Diffusion Lengths > 175 μm in Solution-Grown $CH_3NH_3PbI_3$ Single Crystals. *Science* **2015**, *347*, 967−970.
(4) Stranks, S. D.; Eperon, G. E.; Grancini, G.; Menelaou, C.; Alcocer, M. J. P.; Leijtens, T.; et al. Electron-Hole Diffusion Lengths Exceeding 1 Micrometer in an Organometal Trihalide Perovskite Absorber. *Science* **2013**, *342*, 341−344.
(5) De Wolf, S.; Holovsky, J.; Moon, S. J.; Löper, P.; Niesen, B.; Ledinsky, M.; Haug, F. J.; Yum, J. H.; Ballif, C. Organometallic Halide Perovskites: Sharp Optical Absorption Edge and its Relation to Photovoltaic Performance. *J. Phys. Chem. Lett.* **2014**, *5*, 1035−1039.
(6) Xing, G.; Mathews, N.; Sun, S.; Lim, S. S.; Lam, Y. M.; Grätzel, M.; et al. Long-Range Balanced Electron- and Hole-Transport Lengths in Organic-Inorganic $CH_3NH_3PbI_3$. *Science* **2013**, *342*, 344−347.
(7) Green, M. A.; Ho-Baillie, A.; Snaith, H. J. The Emergence of Perovskite Solar Cells. *Nat. Photonics* **2014**, *8*, 506−514.
(8) Nouri, E.; Wang, Y. L.; Chen, Q.; Xu, J. J.; Paterakis, G.; Dracopoulos, V.; Xu, Z. X.; Tasis, D.; Mohammadi, M. R.; Lianos, P. Introduction of Graphene Oxide as Buffer Layer in Perovskite Solar Cells and the Promotion of Soluble n-Butyl-substituted Copper Phthalocyanine as Efficient Hole Transporting Material. *Electrochim. Acta* **2017**, *233*, 36−43.
(9) Nouri, E.; Krishna, J. V. S.; Kumar, C. V.; Dracopoulos, V.; Giribabu, L.; Mohammadi, M. R.; Lianos, P. Soluble tetratriphenyl-amine Zn phthalocyanine as Hole Transporting Material for Perovskite Solar Cells. *Electrochim. Acta* **2016**, *222*, 875−880.

(10) Domanski, K.; Correa-Baena, J. P.; Mine, N.; Nazeeruddin, M. K.; Abate, A.; Saliba, M.; Tress, W.; Hagfeld, A.; Grätzel, M. Not All That Glitters Is Gold: Metal-Migration- Induced Degradation in Perovskite Solar Cells. *ACS Nano* **2016**, *10*, 6306−6314.

(11) Habisreutinger, S. N.; Leijtens, T.; Eperon, G. E.; Stranks, S. D.; Nicholas, R. J.; Snaith, H. J. Carbon Nanotube/Polymer Composites as a Highly Stable Hole Collection Layer in Perovskite Solar Cells. *Nano Lett.* **2014**, *14*, 5561−5568.

(12) Guarnera, S.; Abate, A.; Zhang, W.; Foster, J. M.; Richardson, G.; Petrozza, A.; Snaith, H. J. Improving the Long-Term Stability of Perovskite Solar Cells with a Porous Al_2O_3 Buffer-Layer. *J. Phys. Chem. Lett.* **2015**, *6*, 432−437.

(13) Li, W.; Dong, H.; Wang, L.; Li, N.; Guo, X.; Li, J.; Qiu, Y. Montmorillonite as Bifunctional Buffer Layer Material for Hybrid Perovskite Solar Cells with Protection from Corrosion and Retarding Recombination. *J. Mater. Chem. A* **2014**, *2*, 13587−13592.

(14) Jia, X.; Zhang, L.; Luo, Q.; Lu, H.; Li, X.; Xie, Z. Z.; Yang, Y.; Li, Y. Q.; Liu, X.; Ma, C. Q. Power Conversion Efficiency and Device Stability Improvement of Inverted Perovskite Solar Cells by Using a ZnO:PFN Composite Cathode Buffer Layer. *ACS Appl. Mater. Interfaces* **2016**, *8*, 18410−18417.

(15) Wei, W.; Hu, Y. H. Catalytic Role of H_2O in Degradation of Inorganic−Organic Perovskite ($CH_3NH_3PbI_3$) in Air. *Int. J. Energy Res.* **2017**, *41*, 1063−1069.

(16) Grossiord, N.; Kroon, J. M.; Andriessen, R.; Blom, P. W. M. Degradation Mechanisms in Organic Photovoltaic Devices. *Org. Electron.* **2012**, *13*, 432−456.

(17) Hashmi, S. G.; Martineau, D.; Dar, M. I.; Myllymaki, T. T. T.; Sarikka, T.; Ulla, V.; Zakeeruddin, S. M.; Gratzel, M. High Performance Carbon-Based Printed Perovskite Solar Cells with Humidity Assisted Thermal Treatment. *J. Mater. Chem. A* **2017**, *5*, 12060−12067.

(18) Ryu, J.; Lee, K.; Yun, J.; Yu, H.; Lee, J.; Jang, J. Paintable Carbon-Based Perovskite Solar Cells with Engineered Perovskite/Carbon Interface Using Carbon Nanotubes Dripping Method. *Small* **2017**, No. 1701225.

(19) Chen, H.; Yang, S. Carbon-Based Perovskite Solar Cells without Hole Transport Materials: The Front Runner to the Market? *Adv. Mater.* **2017**, No. 1603994.

(20) Nouri, E.; Mohammadi, M. R.; Lianos, P. Inverted Perovskite Solar Cells Based on Lithium-Functionalized Graphene Oxide as an Electron-Transporting Layer. *Chem. Commun.* **2017**, *53*, 1630−1633.

(21) Nouri, E.; Mohammadi, M. R.; Lianos, P. Improving the Stability of Inverted Perovskite Solar Cells under Ambient Conditions with Graphene-based Inorganic Charge Transporting Layers. *Carbon* **2018**, *126*, 208−214.

(22) Cao, J.; Yu, H.; Zhou, S.; Qin, M.; Lau, T. K.; Lu, X.; Zhao, N.; Wong, C. P. Low-Temperature Solution-Processed NiO_x Films for Air-Stable Perovskite Solar Cells. *J. Mater. Chem. A* **2017**, *5*, 11071−11077.

(23) Islam, M. B.; Yanagida, M.; Shirai, Y.; Nabetani, Y.; Miyano, K. NiO_x Hole Transport Layer for Perovskite Solar Cells with Improved Stability and Reproducibility. *ACS Omega* **2017**, *2*, 2291−2299.

(24) Yao, K.; Lic, F.; Hea, Q.; Wang, X.; Jiang, Y.; Huang, H.; Jen, A. K.-Y. A copper-doped nickel oxide bilayer for enhancing efficiency and stability of hysteresis-free inverted mesoporous perovskite solar cells. *Nano Energy* **2017**, *40*, 155−162.

(25) Kim, J. H.; Liang, P.-W.; Williams, S. T.; Cho, N.; Chueh, C.-C.; Glaz, M. S.; Ginger, D. S.; Jen, A. K.-Y. High-Performance and Environmentally Stable Planar Heterojunction Perovskite Solar Cells Based on a Solution-Processed Copper-Doped Nickel Oxide Hole-Transporting Layer. *Adv. Mater.* **2015**, *27*, 695−701.

(26) Garcia-Belmonte, G.; Munar, A.; Barea, E. M.; Bisquert, J.; Ugarte, I.; Pacios, R. Charge Carrier Mobility and Lifetime of Organic Bulk Heterojunctions Analyzed by Impedance Spectroscopy. *Org. Electron.* **2008**, *9*, 847−851.

(27) Bisquert, J.; Santiago, F. F.; Sero, I. M.; Belmonte, G. G.; Gimenez, S. Electron Lifetime in Dye-Sensitized Solar Cells: Theory and Interpretation of Measurements. *J. Phys. Chem. C* **2009**, *113*, 17278−17290.

(28) Nouri, E.; Mohammadi, M. R.; Lianos, P. Impact of Preparation Method of TiO_2-RGO Nanocomposite Photoanodes on the Performance of Dye-Sensitized Solar Cells. *Electrochim. Acta* **2016**, *219*, 38−48.

(29) Hummers, W.; Offeman, R. Preparation of Graphitic Oxide. *J. Am. Chem. Soc.* **1958**, *80*, 1339.